Received: 18 September 2023 | Revised: 13 January 2024 | Accepted: 28 January 2024

DOI: 10.1002/rra.4256

RESEARCH ARTICLE

WILEY

Remotely sensed land-cover change and floodplain disturbance following upstream-migrating river avulsions in tropical rainforests

Riley T. Henson [1,2] | Douglas A. Edmonds [1] | Eli D. Lazarus [3]

[1]Department of Earth and Atmospheric Sciences, Indiana University, Bloomington, Indiana, USA

[2]Department of Geosciences, University of Montana, Missoula, Montana, USA

[3]Environmental Dynamics Lab, School of Geography and Environmental Science, University of Southampton, Southampton, UK

Correspondence
Douglas A. Edmonds, Department of Earth and Atmospheric Sciences, Indiana University, Bloomington, IN, USA.
Email: edmondsd@indiana.edu

Funding information
National Science Foundation

Abstract

The displacement of a river to a new position within its adjacent floodplain is called avulsion, and here we examine how a newly recognized style, called retrogradational avulsion, affects the surrounding floodplain in tropical rainforests using remote sensing. Retrogradational avulsions begin with a channel blockage that causes self-propagating upstream dechannelization and flooding. While this flooding results in vegetation die-off and floodplain sedimentation, few quantitative measurements of disturbance by retrogradational avulsions exist. Here, we first focus on land-cover change following a single retrogradational avulsion in Papua New Guinea from 2012 to 2021. During the avulsion, the river dechannelized 892 m upstream, and the parent channel width doubled. Using maximum likelihood image classification, we observed healthy vegetation fluctuated around 4.3 km^2, vegetation regrowth peaked in 2017 at 3.2 km^2, dead vegetation peaked in 2013 at 2.1 km^2, and visible extent of deposited sediment was greatest in 2015 at 0.44 km^2. We also examined 19 other retrogradational avulsions in Papua New Guinea and South America using NDVI. The area of floodplain disturbance (i.e., vegetation die-off and possible sedimentation) for each avulsion ranged from <1 to >13 km^2 and scaled with the dechannelization area. Comparing our plan-view disturbance results with FABDEM digital-elevation data and ICESat-2 surface elevation measurements, we hypothesize floodplain disturbance extent is a function of topographic relief. Our results also suggest that retrogradational avulsions, on average, perturb larger areas of forest compared to blowdowns, suggesting this might be an important disturbance regime that influences gap-filling regeneration in tropical rainforests.

KEYWORDS
disturbance regime, floodplain disturbance, image classification, land-cover change, NDVI, remote sensing, retrogradational avulsion, tropical rainforests

1 | INTRODUCTION

River avulsions occur when a river occupies or creates a new channel located on the adjacent floodplain or other fluvial landform (Jones & Schumm, 1999). During a river avulsion, exceptional sediment erosion, deposition, and flooding builds floodplain topography over time and influences the patch mosaic structure of vegetation in densely forested environments such as tropical rainforests (Hupp &

Osterkamp, 1985; Kalliola et al., 1991). The sudden influx of flood water and sediment disturbs the floodplain (e.g., oxygen starvation and uprooting) and influences ecological heterogeneity by causing local vegetation die-off (e.g., deadwood, woody debris, and devegetated patches). Subsequent colonization of pioneer species in open, bare areas created by flooding, scouring, and sediment deposition initiates the turnover of plant communities, leading to primary and secondary succession of vegetation on the forest floor (Battisti et al., 2016; Gullison et al., 1996). Avulsions also affect built environments and can cause catastrophic damage to infrastructure and populations. For example, an avulsion on the Indus River in July 2010 displaced 20,000,000 people and caused nearly 2,000 fatalities (Brakenridge et al., 2017; Syvitski & Brakenridge, 2013). Exactly how avulsions affect the geomorphology and ecology of fluvial systems depends on where they occur and their pattern of movement across the floodplain.

The long-term cause and occurrence of avulsions in fluvial systems are due to sediment deposition on the channel bed (Brooke et al., 2022). This so-called setup phase, the conditioning of a river through fluvial processes that predispose the river for avulsion, marks the long-term aggradation of sediments onto the channel bed. This natural build-up of alluvium causes the alluvial ridge of the channel to rise above the surrounding floodplain. The channel becomes gravitationally unstable when its bed elevation roughly matches the floodplain elevation, reaching a state of superelevation (Bridge & Leeder, 1979; Bryant et al., 1995; Hoyal & Sheets, 2009; Jerolmack & Mohrig, 2007; Mohrig et al., 2000). If a large enough trigger occurs, the channel, once superelevated, becomes susceptible to avulsion. The trigger results from a range of processes, usually associated with flooding (Jones & Schumm, 1999; Morón et al., 2017) due to levee breach (Millard et al., 2017; Slingerland & Smith, 1998, 2004) or overbank flow (Edmonds et al., 2009; Field, 2001). The outbreak of water and the associated conveyance of sediment onto the floodplain initiates the avulsion processes after the trigger event.

As an avulsion progresses, sediment and water organize into a new or preexisting channel, characterized by three generally accepted styles: progradation, annexation, and incision (Slingerland & Smith, 2004). Progradational avulsions consist of a downstream-moving sediment wedge or crevasse splay. These wedges contain a network of channels, and the avulsion terminates when a single flow path emerges from the channel network and reconnects to a fluvial system downstream (Flood & Hampson, 2014; Slingerland & Smith, 2004; Smith et al., 1989; Valenza et al., 2020). Incisional avulsions occur when water flows toward topographic lows and incises into the floodplain, developing a new channel that captures flow and sediment from the parent channel (Hajek & Edmonds, 2014; Mohrig et al., 2000; Slingerland & Smith, 2004). Annexational avulsions, in contrast, reoccupy pre-existing active or inactive river channels on the floodplain (Edmonds et al., 2016; Slingerland & Smith, 2004; Valenza et al., 2020).

Recently, researchers have identified a new, fourth style of river avulsion. Edmonds et al. (2022) and Lombardo (2017) identified upstream-migrating avulsions in the tropical rainforests of Papua New Guinea and South America that dechannelize and self-propagate upstream over time as they find a new flow path. These so-called retrogradational avulsions are most likely initiated by a channel blockage, such as a logjam, though this has never been conclusively observed. The blockage causes a local backwater that raises the water level upstream, leading to water spilling overbank. The overbank flow creates a chevron-shaped flooding pattern on the forest floor, subsequently depositing sediment and killing vegetation (e.g., woody material and grass) (Edmonds et al., 2022; Figure 1a). As water spills overbank, discharge in the channel decreases and flow decelerates near the blockage, causing sediment to aggrade on the channel bed, filling the channel and forcing the wave of dechannelization to migrate upstream (Figure 1b). The wave of upstream-migrating dechannelization continues until overbank flow establishes a new flow path by either incision or annexation (Figure 1c,d).

All avulsion styles disturb the floodplain and change land-cover through time by flooding and associated hydrosedimentological processes that cause vegetation die-off and shape floodplain architecture. These disturbances impact the spatiotemporal distribution of surrounding ecological biodiversity (Assine et al., 2016; Richards et al., 2002; Stanford et al., 2005; Tockner et al., 2010; Valente et al., 2013; Valenza et al., 2022; Van Asselen et al., 2017; Ward et al., 2002). Progradational avulsions create widespread floodplain disturbance from flooding and sediment deposition, and annexational or incisional avulsions result in little floodplain disturbance as they only reoccupy pre-existing channels (Valenza et al., 2020, 2022). Comparatively, disturbances from retrogradational avulsions remain underexamined, and while some studies exist (Edmonds et al., 2022; Gullison et al., 1996; Lombardo, 2017; Valenza et al., 2022), a need for basic information regarding the characteristic size of disturbance and the mechanics of the avulsion process remains.

In this paper, we quantitatively describe planimetric areal extents of disturbance that retrogradational avulsions leave on the floodplain (measured in square meters/kilometers). Recently, the use of high- to medium-resolution and multispectral satellite imagery has transformed our understanding of river avulsions, capturing remotely sensed data of the avulsion process at multiple temporal and spatial scales useful for morphological and ecological observations (Brooke et al., 2022; Buehler et al., 2011; Edmonds et al., 2016; Iacobucci et al., 2020; Lee et al., 2022; Valenza et al., 2022). Additionally, historical remote sensing data has proven to be a critical tool in assessing both small- and large-scale (<0.001 and >0.001 km^2, respectively) disturbances in forests (Frolking et al., 2009). Following this methodology, we used high-resolution eight-band multispectral WorldView-2 satellite imagery and a maximum likelihood image classification method in ERDAS Imagine to investigate the retrogradational avulsion process at a fine spatiotemporal scale of a single river in Papua New Guinea (avulsion R3.2 from Edmonds et al., 2022). To look more broadly at how these avulsions disturbed the floodplain, we used harmonized NDVI Landsat imagery of 19 retrogradational avulsions in Google Earth Engine (GEE), a multi-petabyte cloud storage platform composed of global temporal satellite imagery expanding more than 40 years (Kumar & Mutanga, 2018). We aim to describe retrogradational avulsions and the disturbances they create on the surrounding floodplain.

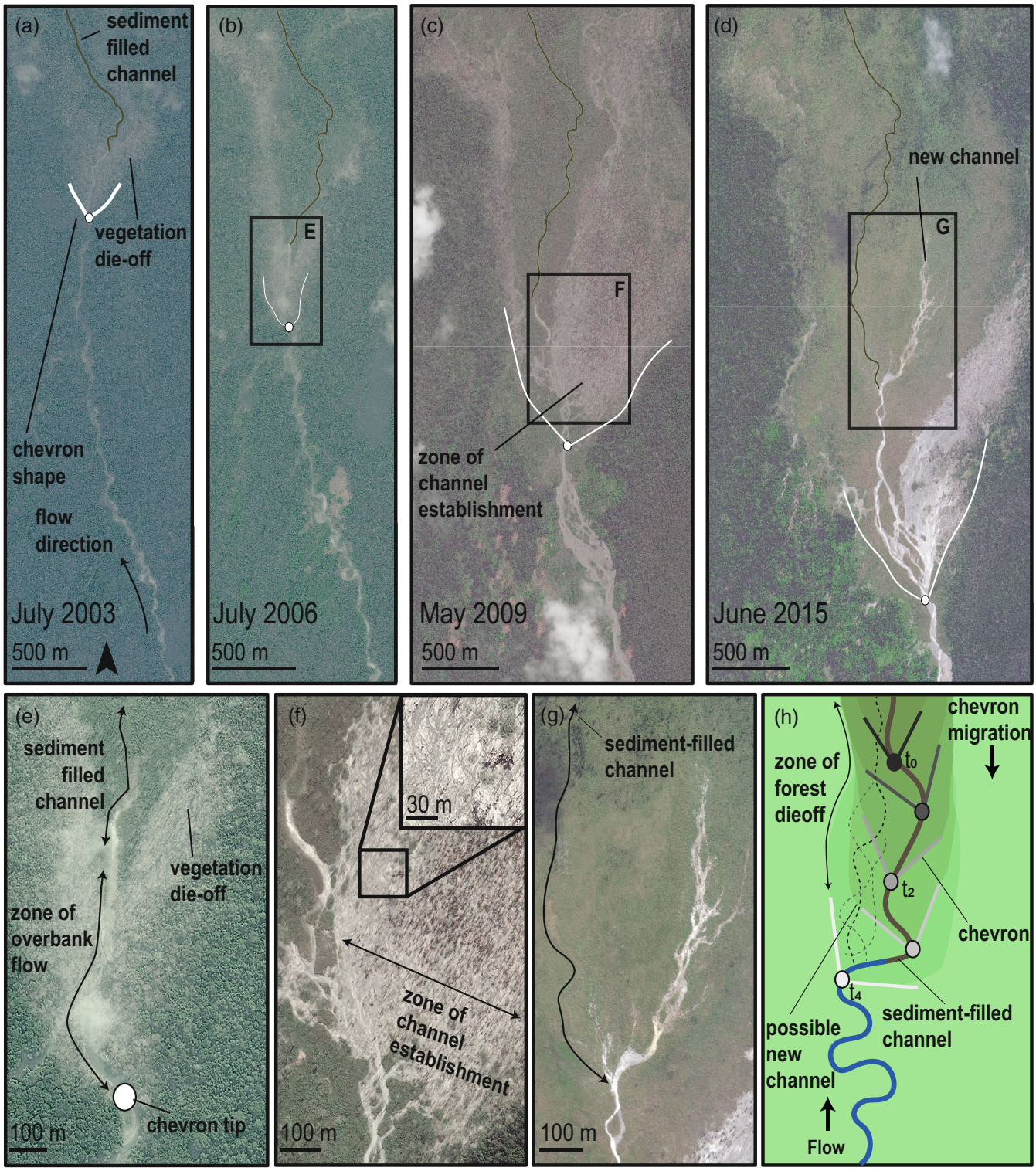

FIGURE 1 Temporal evolution of a retrogradational avulsion in Papua New Guinea (R3.2) (a–g). Schematic representation of R3.2 through time depicting temporally banded chevrons (h). The tip of the chevron in (a) is at 9.435°S, 149.095°E. Figure from Edmonds et al. (2022). [Color figure can be viewed at wileyonlinelibrary.com]

2 | METHODS

2.1 | Study areas

Edmonds et al. (2022) created a dataset of 69 retrogradational avulsions. Using their data, we looked at 20 avulsions that had sufficient satellite imagery to study the associated land-cover change and floodplain disturbance. The avulsions in this study occurred in Papua New Guinea and the Amazon Basin. Two avulsions (including R3.2, studied in detail) were in Papua New Guinea north of Mt. Suckling, part of the Owen Stanley Range, in Oro (Northern) Province. These two avulsion

sites were in the Papuan Peninsula covered by the Southeastern Papuan rain forests that are of the tropical and subtropical moist broadleaf biome (Olson et al., 2001). The mean annual temperature ranges from 24 to 27°C and the average yearly precipitation is >2,500 mm, with the heaviest rainfall occurring in the highlands (World Bank Group, 2022). We used the 30 arc-second climate dataset WorldClim to estimate the temperature values, which contained global climate data from 1970 to 2000 (Hijmans et al., 2005). The avulsion activity in Papua New Guinea occurred at 36–45 m above sea level (Figure 2a).

The remaining 18 avulsions occurred in the northeastern foothills of the Andean Mountains, with one in Madre de Dios, Peru (R15), and 17 distributed throughout the Beni and La Paz plains in Bolivia. All 18 avulsions were in the southwestern Amazon Rainforest Ecotone, an ecologically diverse region between the terra firme rainforest of the Amazon and the tropical savannahs of the Moxos plains in Bolivia (Maezumi et al., 2022). Specifically, the avulsions were in the densely vegetated ecoregions of the Southwest Amazon moist forests and Bolivian Yungas, both of which are composed of tropical and subtropical moist broadleaf forest biomes (Olson et al., 2001). The mean annual temperature ranges from 22 to 27°C and the precipitation varies between 1500 and 2100 mm per year (Singh et al., 2022). The avulsion activity in South America occurred at 180–280 m above sea level (Figure 2b).

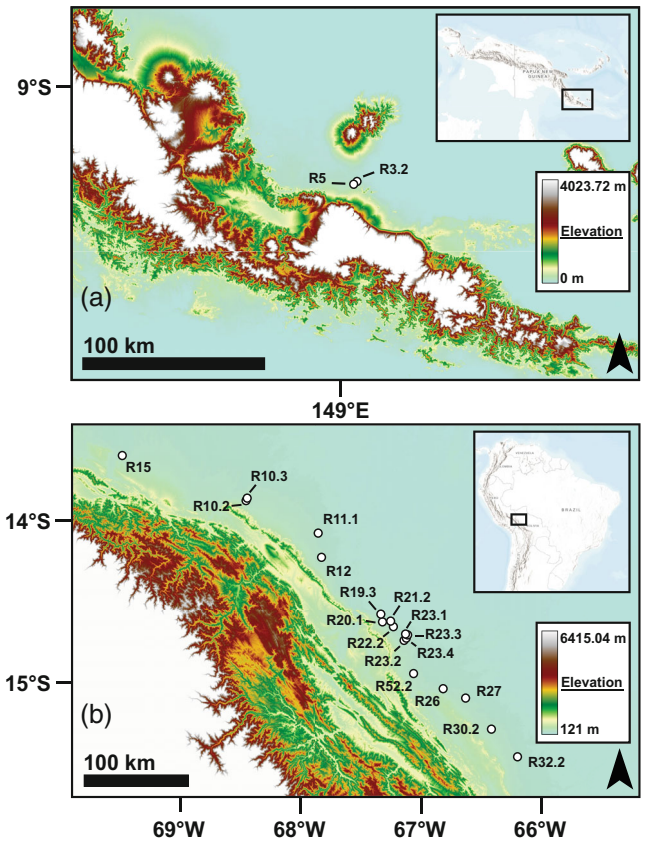

FIGURE 2 Locations of retrogradational avulsions in this study in Papua New Guinea (a) and parts of South America (b). Avulsion IDs are from Edmonds et al. (2022). Elevation data were acquired by the FABDEM (Hawker et al., 2022). [Color figure can be viewed at wileyonlinelibrary.com]

2.2 | Land-cover change and floodplain disturbance

2.2.1 | High-resolution examination of R3.2

The R3.2 avulsion in Papua New Guinea migrated upstream from 2002 to 2014 (Edmonds et al., 2022). We chose to study this avulsion in detail because it had the most expansive multi-temporal high-resolution data available, with seven WorldView-2 high-resolution 8-band multispectral satellite images, collected from Maxar Technologies, that record its later evolution. This satellite provided images with 1.8–2.0 m resolution with eight spectral bands covering the visible to near-infrared spectrum. We found only seven suitable images of this avulsion due to the high cloud coverage within the satellite archive. The images used were captured on 4 April 2012, 5 April 2013, 3 November 2013, 12 May 2014, 24 August 2015, 9 August 2017, and 30 June 2021.

We used ERDAS IMAGINE 2018 (64-bit) to create supervised maximum likelihood image classifications for each WorldView-2 image to observe the geomorphic and ecological signatures of land-cover change associated with the retrogradational avulsion. The maximum likelihood classifier is widely used because it chooses the most probable spectral class, has a computationally efficient algorithm, can account for natural variation in spectral patterns, and has high accuracy over variable conditions and environments (Bolstad & Lillesand, 1991). The classifier assumes normally distributed spectral data and calculates the mean and variance of each class to estimate the highest probability for each pixel.

We clipped the seven images to focus on the avulsion area to reduce noise in the classifier and oversampling of background features. Based on the visual inspection of this avulsion, we subdivided land-cover change into seven spectral class types associated with healthy vegetation, low-lying vegetation (e.g., grasses) that we referred to as "regrowth," vegetation die-off (e.g., deadwood, woody debris, and devegetated patches), sediment, water, clouds, and unclassified areas. To define each class, we selected multiple polygons that covered the land-cover class type. For each image, we had to augment our procedure because the classes showed a large spectral range due to natural noise and variable sizes of specific land-cover. Since the maximum likelihood classifier assigns pixel values based on the mean and variance calculated by the program, pixels outside these statistics due to the large spread of values were inaccurately assigned. The augmented procedure consisted of subdividing the spectral distribution into multiple classes and selecting multiple polygons for each subdivided class; therefore, the final class was the combination of the subdivided classes. For each image, the first subdivided class for a given spectral class type contained 20 sample polygons. Each subsequent subdivided class contained five sample polygons until the classifier

produced satisfying visual inspections and accuracy assessment values.

We assessed the accuracy with two different methods. For the first assessment, we used a stratified random sampling method with 250 validation points for each image and for the second assessment, we used an equalized random sampling method using five validation points for each class. Validation points were identified visually in the high-resolution images. The stratified random sampling method emphasized the representation of the larger classes (i.e., healthy vegetation, vegetation regrowth within the chevron, and vegetation die-off), and the equalized random sampling method assured a representation of the smaller classes (i.e., water and deposited sediment). For each assessment, we measured the overall accuracy (OA) and Cohen's kappa coefficient (K) as the final accuracy scores. We continued image classification until accuracy assessment scores reached 90% or greater for OA and 0.90 or greater for K (Congalton, 1991).

In addition to the image classification method, we measured avulsion morphometrics of the retrogradational avulsion in Papua New Guinea (R3.2) using ArcGIS Pro. We first measured the cumulative sediment plug migration from 2003 to 2009 by tracking the distance it moved upstream from one image to another. We then measured the average channel width from 2003 to 2021 by averaging 19 times at three different cross-sections ~5 km upstream of the final chevron tip position.

2.2.2 | Medium-resolution examination of 19 retrogradational avulsions

We focused on 19 retrogradational avulsions throughout Papua New Guinea and South America based on available 30 m resolution Landsat 5, 7, and 8 images without cloud cover and anthropogenic influences (e.g., agricultural land and preexisting unvegetated land) using GEE. Due to the lack of suitable high-resolution Maxar images for these avulsions, a detailed examination of land-cover classification was impossible. Instead, we used Landsat to get a first-order assessment of the total floodplain disturbance (i.e., vegetation die-off and possible sedimentation) caused by the upstream-migrating wave of flooding. In this way, the area measured was a minimum value of the floodplain disturbance as there might have been sub-canopy disturbances that did not always create vegetation die-offs.

To analyze the floodplain disturbance, we created composite images from all suitable Landsat data during each retrogradational avulsion (time periods reported in Edmonds et al., 2022). For the composite images, we harmonized atmospherically corrected Landsat 5, 7, and 8 Surface Reflectance Tier 1 images (Figure 3a). We corrected the spectral differences in the different Landsat sensors using coefficients provided by Roy et al. (2016) that harmonized the Landsat 5, 7, and 8 satellite archives into one image collection spanning from 1984 to the present developed from the GEE platform (https://developers.google.com/earth-engine/tutorials/community/landsat-etm-to-oli-harmonization). The harmonization of the three sensors reduced error produced by the Landsat 7 ETM+ SLC-off data and cloud coverage, while also providing a longer observational period spanning nearly four decades. To further reduce the error produced by the presence of clouds in images, we applied a cloud mask and cloud cover filter to each composite.

With a harmonized image collection, we spectrally transformed all data into normalized difference vegetation index (NDVI) images to visualize the floodplain or vegetation disturbance and performed a 10th percentile reducer to select only "disturbed" pixels for a given location within an image stack (Figure 3b). To capture different phases of disturbance, we subdivided the avulsion duration into 2-year periods (Figure 3b2–4). This meant a single avulsion contained multiple 2-year composites, anywhere from three (e.g., R11.1) to 16 (e.g., R12). On each 2-year composite, we manually adjusted an NDVI classification threshold to isolate the disturbed pixels and clipped the thresholded area of interest (Figure 3, where b1 is b5 + b6 + b7). The threshold varied for each avulsion, but it generally ranged from NDVI <0.6 to 0.75. The final step included mosaicking the 2-year thresholded composites into a single composite to contain the total disturbance area caused by the avulsion (Figure 3c). Due to cloud cover variability among years, we divided some composites into one-year periods and then mosaicked them into a regular 2-year period composite (e.g., we mosaicked 2016–2017 and 2017–2018 1-year composite periods to form the 2-year composite period 2016–2018 for R10.3). Additionally, some 2-year composite periods may actually contain a 1-year composite period but represent the area of floodplain disturbance in a 2-year period (e.g., R10.2 had a 1-year composite period from 1994 to 1995 but had total floodplain disturbance representation from 1994 to 1996 due to 1996 resulting in no new disturbance and greater cloud coverage in the area of interest), and we thus recorded it as a 2-year composite in our analysis for methodological continuity.

3 | RESULTS

3.1 | Detailed examination of land-cover change from avulsion R3.2

We performed an in-depth study of retrogradational avulsion R3.2 in Papua New Guinea. The avulsion began in 2002, but our high-resolution satellite image collection started in 2012 and by 2021 the river started re-establishing itself into a new channel on the floodplain farther downstream. On each image, we first measured the geometry and morphodynamics of the river channel to gain insight as to how the avulsion style affects the channel itself and then examined the floodplain disturbance from 2012 to 2021.

3.1.1 | Channel setting and morphodynamics

In satellite imagery, the most conspicuous and observable phase of the retrogradational avulsion is the upstream-migrating wave

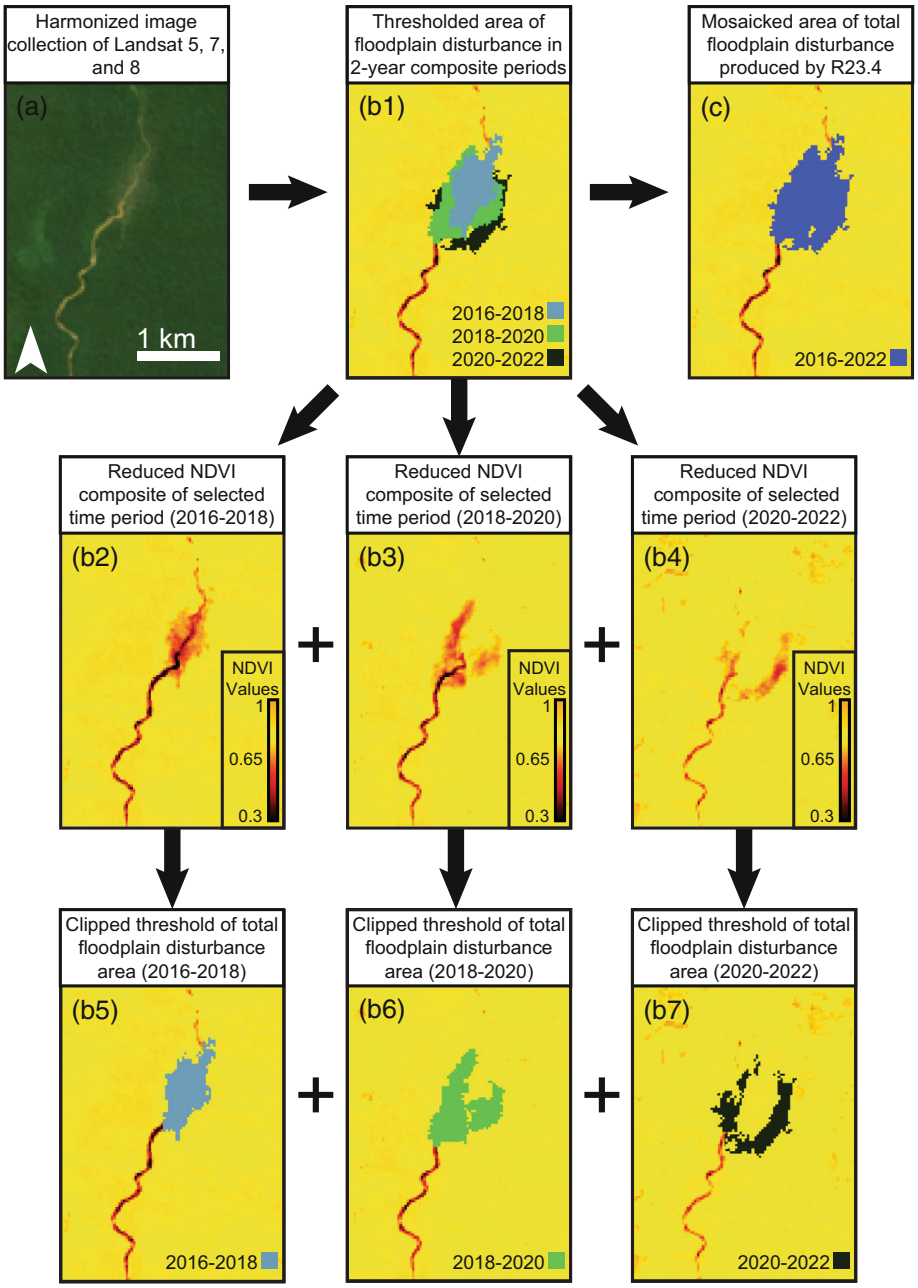

FIGURE 3 Workflow to measure the total floodplain disturbance area. An example shown is R23.4 from Edmonds et al. (2022). (a) We harmonized all Landsat 5, 7, and 8 images into one collection. (b1) Spectrally transformed 2-year composites that selected all pixels that were disturbed by the avulsion. In this example, there were three 2-year composite periods that captured the total disturbance. To create b1, we transformed each 2-year composite into NDVI (b2–4). Then, we applied a classification threshold to isolate avulsion-related "disturbed" pixels (b5–7). To create b1, we added b5 + b6 + b7, which superimposed the youngest composite over the oldest. (c) The mosaicked total area of floodplain disturbance. [Color figure can be viewed at wileyonlinelibrary.com]

of dechannelization. Interestingly, the upstream-migrating wave of dechannelization seems to have far-field effects on the parent channel and floodplain over time. On avulsion R3.2, the dechannelization wave moved upstream, water spilled onto the adjacent floodplain and deposited sediment on the flanks of the channel as floodwater expanded and decelerated through the vegetation (Figure 1). Simultaneously, the parent channel itself is filled with sediment. This sediment "plug" probably consisted of rapidly deposited bed material load due to deceleration of flow that resulted in a local backwater upstream of the plug (Edmonds et al., 2022). The movement of the sediment plug upstream defined the key characteristic of this feedback loop as it forced flooding and overall avulsion activity. From 2003 to 2009, the plug migrated upstream 892 m (Figures 1 and 4a). Our measurements indicated an unsteady rate of plug migration. From 2003 to late 2004, the sediment plug had an upstream migration rate of 71 m/yr, whereas from 2005 to mid-2006, the plug migration rate increased to 297 m/yr, and then from 2006 to 2009, the rate of upstream migration decreased to approximately 113 m/yr. Note that plug movement stopped after 2009 as the channel selected a new flow path on the floodplain.

The width of the parent channel increased in response to the dechannelization wave, but it lagged behind by about 2–3 years (Figure 4b). From 2003 to 2005, the channel width had a constant average width of 29 m. Then from 2005 to 2013, the width linearly increased from 34 to 60 m in 8 years. After 2013, the average channel width eventually stabilized at 60 m.

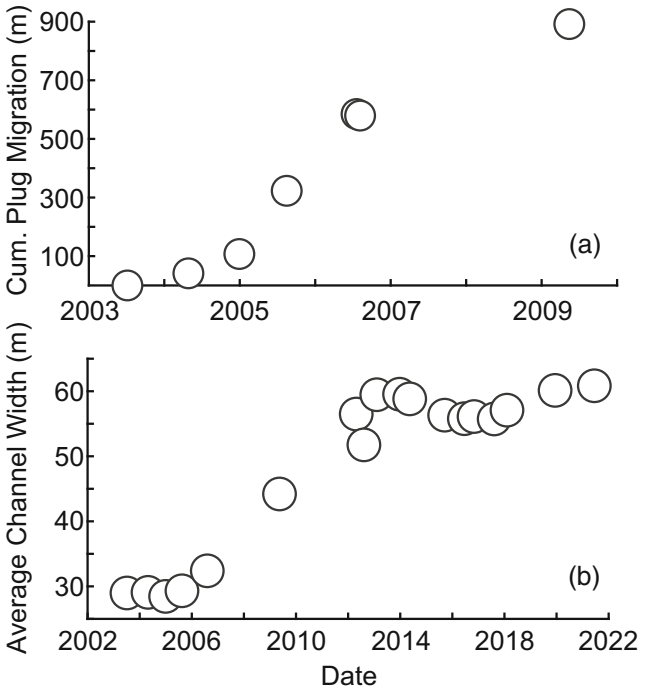

FIGURE 4 Cumulative distance of upstream sediment plug migration from 2003 to 2009 (a) and average channel width measured upstream of the avulsion from 2003 to 2021 (b).

3.1.2 | Land-cover change through time

Additionally, we mapped the land-cover change associated with R3.2 from 2012 to 2021. In each image, we classified healthy vegetation, vegetation die-off, vegetation regrowth within the chevron, sediment, water, and clouds (Figure 5). In general, the land-cover changes appear to agree with observations by Edmonds et al. (2022) in that the retrogradational avulsion is comprised of distinct phases. Whereas Edmonds et al. (2022) only distinguished between two phases—upstream-migrating dechannelization and pathfinding—we further subdivide those into flooding, channel breakout, channel establishment, and stabilization. The first two are part of the upstream migration and the latter two are part of pathfinding.

The first phase, flooding, initiates floodplain disturbance. In Figure 5a, we observed the floodplain 10 years after avulsion initiation and the predominant features included the areas of vegetation regrowth (1.5 km^2) and deposited sediment in the parent channel downstream of the active avulsion site (0.07 km^2). A year later in 2013, flow dechannelized again, forming a chevron-shaped flooding pattern, killing 1.7 km^2 of vegetation in the diagnostic chevron shape, resulting in over 900% increase in vegetation die-off from the previous image (Figure 5b). The chevron, classified by the red pixels, showed that the vegetation die-off roughly equaled that on either limb of the chevron in surface area, possibly indicating equal distribution of floodwaters to either side.

We observed that channel breakout and channel establishment coincided with each other. In 2013, the channel breakout phase of the avulsion began once the fluvial levee breach resulted in a crevasse splay (Figure 5c). This caused vegetation disturbance with alluvial sediment deposition on the floodplain; healthy vegetation had its lowest extent with only 3.7 km^2 on the floodplain, and 0.41 km^2 of exposed sediment covered the forest floor (Figure 5d). As flow diverted onto the floodplain at the breakout location, alluvial sediment deposited on the forest floor (Figure 5d). The crevasse splay contained a multithread water flow that scoured the floodplain between trees and other vegetation, predisposing a zone on the floodplain for channel establishment. Vegetation die-off experienced a sharp decline (0.7 km^2), healthy vegetation increased (5.1 km^2), and deposited sediment also increased (0.44 km^2) in the following year (Figure 5e). Sediment nearly covered all the splay area, and the scour channels filled with sediment. Once sediment choked the zone of channel establishment to divert the flow path downstream, the river rechannelized, marking avulsion termination. Confined within the sediment-filled parent channel in the middle of vegetation regrowth, avulsion-induced floodplain sedimentation halted and water flowed downstream, forming a single-threaded meandering channel.

When the channel establishment terminated, the stabilization phase began. Figure 5f,g show large vegetation regrowth surface areas (3.2 and 2.21 km^2, respectively) with minimal vegetation die-off (0.47 and 0.23 km^2, respectively) within the forest canopy gap created by the avulsion. Rainforest growth completely covered the sediment-rich zone of channel establishment by 2021, and we observed minimal vegetation die-off with a decrease in vegetation regrowth. The flow continued to incise into the floodplain while gradually forming a meandering and fully channelized flow path farther downstream.

Over time, these changes revealed patterns on the floodplain (Figure 6). During flooding (phase A), dead vegetation increased at the highest rate measured with minimal sediment deposited. Channel breakout (phase B) contained peak vegetation die-off in 2013, a steep decrease in healthy vegetation, rapid sediment deposition, and a continued increase in regrowth. Channel establishment (phase C) marked the highest area of healthy vegetation with a decrease in regrowth, peak sedimentation in 2015, and a rapid decrease in die-off. Stabilization (phase D) primarily consisted of nearly nonexistent deposited sediment and die-off by 2021, with a steady rate of healthy vegetation and a decrease in regrowth.

3.2 | Examination of floodplain disturbance across 19 different avulsions

The most conspicuous change associated with R3.2, and from visible inspection of other retrogradational avulsions, is the immense floodplain and forest disturbance that occurs during flooding and dechannelization. On R3.2, this disturbance perturbed forest ecology and provided a minimum area over which flooding and sediment deposition occurred. We looked at 19 other retrogradational avulsions worldwide and used Landsat images from Google Earth Engine to measure the total floodplain disturbance (as tracked by dead vegetation and possible sedimentation) created during upstream migration and flooding.

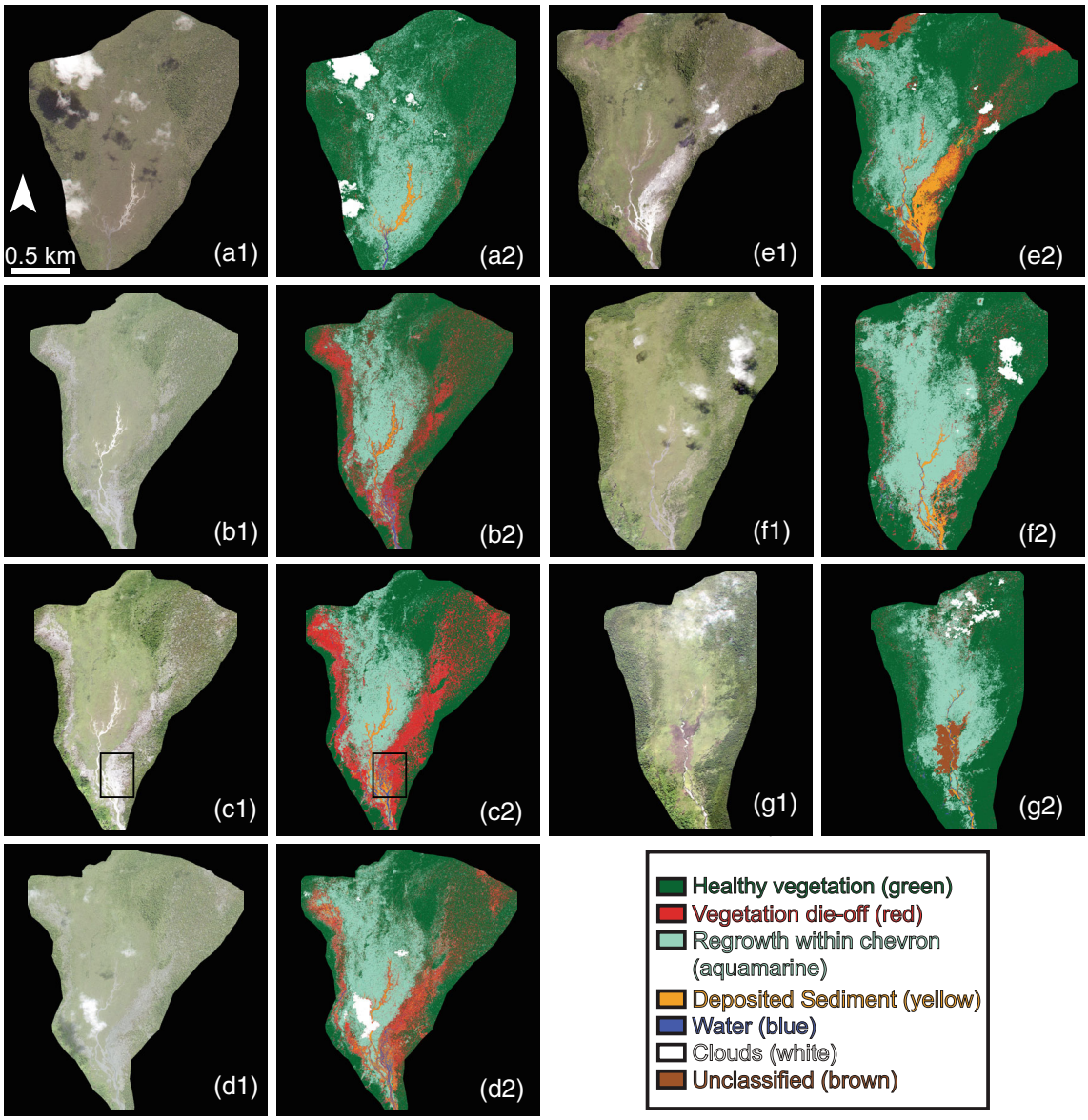

FIGURE 5 Multitemporal eight-band multispectral WorldView-2 satellite images of R3.2 captured on 4 April 2012 (a), 5 April 2013 (b), 23 November 2013 (c), 12 May 2014 (d), 24 August 2015 (e), 9 August 2017 (f), and 30 June 2021 (g) with a RGB band combination of 432 to show natural color (a1–g1) and a thematic map classifying land-cover change derived from supervised maximum likelihood image classification (a2–g2). Rectangle in c1/2 outlines crevasse splay. [Color figure can be viewed at wileyonlinelibrary.com]

For the additional 19 avulsions measured, we classified Landsat images across the retrogradational avulsion date range to create a detailed image and measurable area of the total floodplain disturbance (Figure 7). We visually showed the temporal change in the disturbance area by superimposing earlier composites over later ones, and graphically by plotting the disturbance area for each 2-year period for avulsions with four or more composites. Some of these disturbances showed the classic chevron shape (e.g., R11.1, R22.2, R26, and R23.1), whereas others showed a shape that we described as more confined (R12, R15, and R32.2) or just lacking a pronounced "V" shape (e.g., R23.3 and R30.2). Conceptually, Figure 1h illustrates the classic chevron shape, whereas a confined chevron would be similar except that it exhibits a narrower angle. Over time, nearly all disturbances grew progressively, creating temporally banded chevrons similar to R3.2 (Figure 5). The inset time series showed that the disturbance area fluctuates greatly from year to year (Figure 7).

The total floodplain disturbance for the 19 avulsions had a minimum value of 0.61 km^2 (R20.1), a maximum value of 13.67 km^2 (R12), and mean and median values of 4.54 km^2 and 2.59 km^2, respectively (Figure 8). To compare avulsions that occurred on different-sized rivers, we normalized the disturbance area by dividing it by the dechannelization area within the chevron. We calculated the area by multiplying the dechannelization length by the average river width (Edmonds et al., 2022). The data for the measured (Figure 8a) and

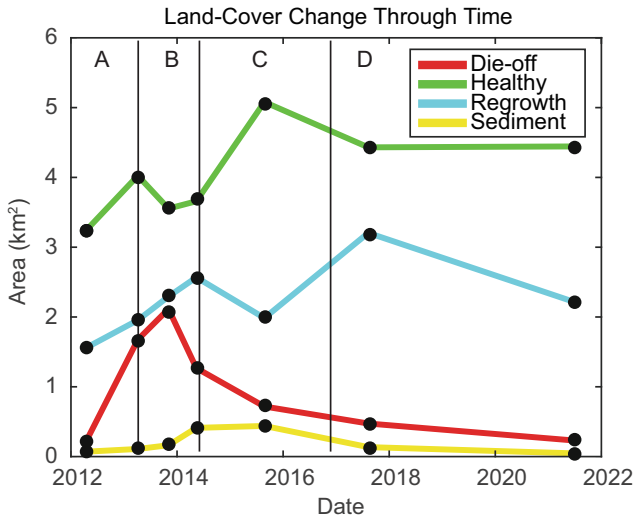

FIGURE 6 Time-series analysis of land-cover change on floodplain plotted from each classified image from 2012 to 2021 including phase boundaries. Phase A is flooding, B is channel breakout, C is channel establishment, and D is stabilization. [Color figure can be viewed at wileyonlinelibrary.com]

normalized (Figure 8b) areas of floodplain disturbance had positively-skewed distributions, with a cluster of data at lower values and few data points at larger values.

The floodplain disturbance area scaled with the dechannelization area within the chevron (Figure 9a). This was not necessarily surprising, since the length of dechannelization (i.e., the channel length within the chevron) limited the size of the avulsion. Additionally, we observed consistent event scaling relationships between the floodplain disturbance perimeter and the floodplain disturbance area (Figure 9b). For this analysis, we focused on avulsion events with three or more images of their disturbance. Any given avulsion generally showed a temporal increase in disturbance area or perimeter as vegetation died followed by a decrease in area or perimeter. We also observed perimeter-area scaling for individual cases of avulsion (Figure 9c). Furthermore, the plots showed that the perimeter area typically grew through time as the avulsion progressed and then shrank as vegetation recovered. These scaling relationships underscored that floodplain disturbance had a consistent morphometry across all measured events.

To investigate other controls on the area of floodplain disturbance, we compared the measured and normalized disturbance areas against four river parameters measured by Edmonds et al. (2022): dechannelization velocity, river discharge (yearly maximum), drainage basin area, and slope. We did this to see if other parameters scaled with floodplain disturbance area produced by the avulsions; however, there were no meaningful trends in the data suggesting the disturbance area was not a function of these river parameters (data not shown). We found avulsion R11.1, located in Bolivia, as an outlier for both river discharge (yearly max) and drainage basin area, and even removing that or other outliers did not create clear trends in the data.

4 | DISCUSSION

4.1 | River and floodplain morphodynamics

Our findings presented new observations associated with the process of retrogradational avulsion. Looking in detail at retrogradational avulsion R3.2 (Edmonds et al., 2022), the upstream-migrating dechannelization wave induced a change in river width (Figure 4b). The avulsion began in 2002, but the channel width remained constant from 2002 to late 2005, indicating a morphological lag of 3 years for width adjustment. Afterward, the channel widened at a rate of 3.25 m/yr, eventually stabilizing when the avulsion selected a new flow path on the floodplain. It was not exactly clear why the channel widened during the upstream-migrating wave of dechannelization, but this is a plausible response to the rapid bed aggradation (Simon & Darby, 1997) caused by the backwater effect or an effect of the frequent floods caused by the sediment plug. It remains unclear how long the channel will remain at the adjusted width, but it appears that the width stabilized at a value double that of the original (29–60 m) as the flow velocity and volume of water and sediment equilibrated to the new river flow path established by the avulsion.

Retrogradational avulsions could efficiently export sediment to the floodplain. Almost all other styles of avulsion involve some amount of channel annexation (i.e., finding a pre-existing flow path) that limits overbank flooding (Valenza et al., 2020, 2022). Retrogradational avulsions seem to always have overbank flooding during the dechannelization process, as evident by the large area of floodplain disturbance and associated vegetation die-offs. Flooding associated with retrogradational avulsion lasts anywhere from less than a year to 36 years (Edmonds et al., 2022), and R3.2 had 12 years of flooding during the avulsion process. This flooding could be hazardous and also export sediment to the floodplain causing aggradation and constructing fluvial levees, possibly leading to larger levees and more floodplain aggradation along the channel reach that experienced dechannelization when compared to the non-disturbed upstream reach.

4.2 | Avulsions as an important mechanism for floodplain disturbance

Although we measured floodplain disturbance differently than land-cover change in the R3.2 study, the 19 retrogradational avulsion events were quite similar to R3.2 (our best-documented example of a retrogradational avulsion) in that they visually appeared to have similar phases. These 19 avulsions displayed a comparable sequence of flooding and sedimentation, forming an upstream-advancing chevron that ceased as vegetation gradually reclaimed the disturbed floodplain (Figures 3 and 7). In the imagery of R3.2, we clearly saw the flooding phase caused massive areas of floodplain disturbance that lasted for more than 3 years from 2013 to 2015 (Figure 5b–e). The most conspicuous effects of retrogradational avulsions consisted of floodplain disturbance via large-scale vegetation die-off and possible sedimentation. Our Google Earth Engine results showed the area of total

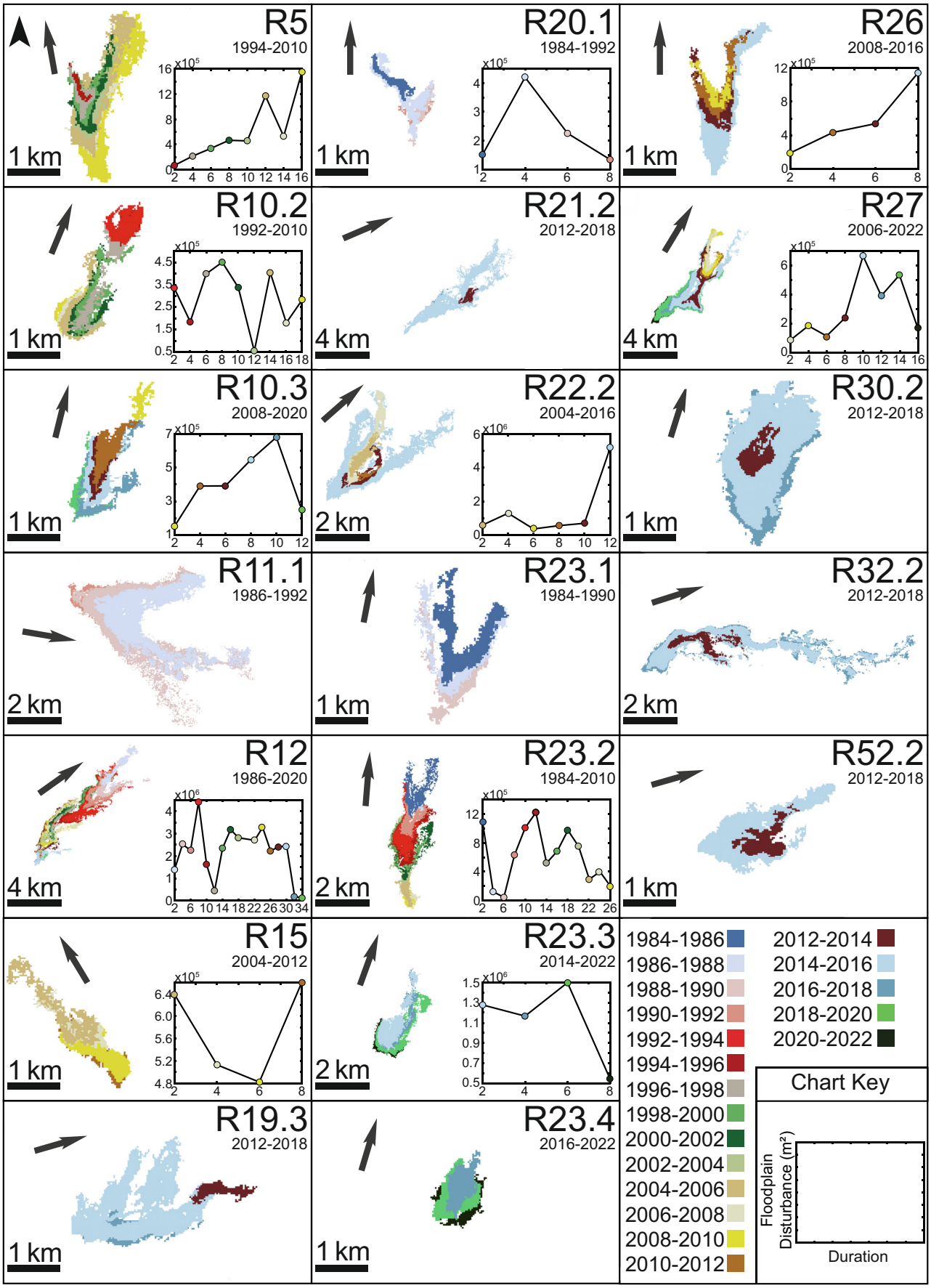

FIGURE 7 Legend on next page.

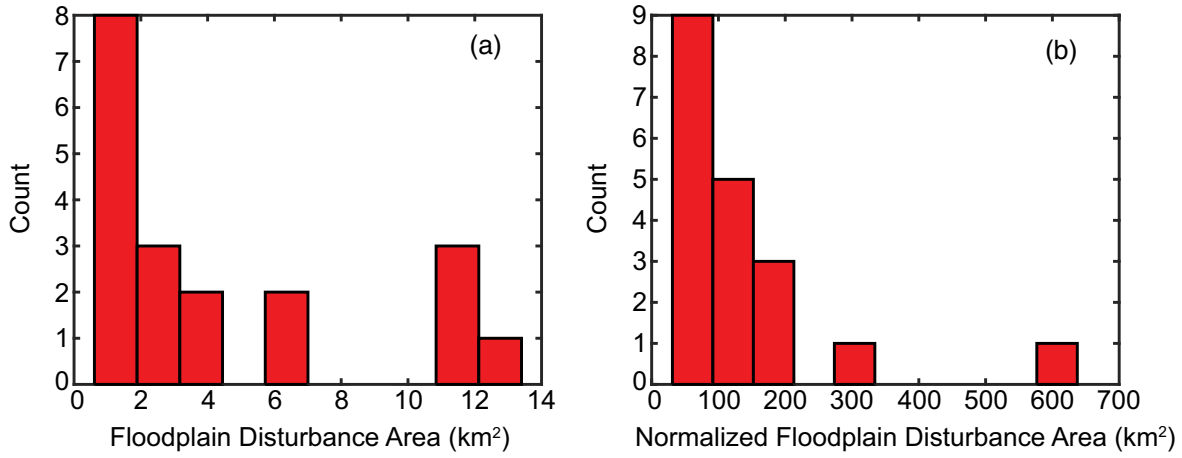

FIGURE 8 Histograms of measured (a) and normalized (b) floodplain disturbance areas produced from 19 retrogradational avulsions measured in Google Earth Engine. [Color figure can be viewed at wileyonlinelibrary.com]

disturbance associated with a single retrogradational avulsion ranged from <1 to >13 km^2, with the largest measured at 13.67 km^2. These large disturbances had unique spatial patterns on the forest floors (Figure 7), with most forming a chevron that has an angled opening downstream of the parent river channel.

These disturbances potentially lead to the ecological succession of pioneer vegetation species that generate diagnostic gap-filling regeneration patterns within the forest canopy (i.e., the stabilization phase). The rivers originating in the Andean mountains in the Amazon are rich in suspended sediment and have high pH and conductivity values (Godoy et al., 1999). During the avulsion, the sediment-rich water flows over the surface of the floodplain and causes localized deposition and erosion on the forest floor, creating patchwork of microhabitats (Godoy et al., 1999; Wittmann et al., 2006). After vegetation die-off, canopy gaps are produced that influence species composition and forest structure (Chambers et al., 2013). The regrowth gives rise to a succession of ecologically biodiverse vegetation, which includes more resistant pioneer species of trees such as mahogany (Gullison et al., 1996). In the disturbed area, there are differing levels of litter depth, nutrient availability, light level, and water availability compared to the surrounding forest, which leads to gap-phase dynamics that bring forth distinct biological mosaics in the Amazon and Southeastern Papua rainforests (Bottero et al., 2011). Due to reduced root and canopy densities in recovering areas, soil water reserves deplete at a slower rate, rainfall interception by overlying vegetation lessens, and light availability with associated localized temperature fluctuation increases (Poorter & Hayashida-Oliver, 2000). The interaction of water and light levels is considered the most important factor influencing dynamics (Myster, 2009; Pires & Prance, 1985), leading to greater height and leaf growth rates within the canopy gap compared to understory plants (Poorter & Hayashida-Oliver, 2000). Canopy openings in tropical rainforests are an important driver of diversification as they control the light levels and soil nutrient/moisture content of the forest gap, prompting dormant seeds in the forest soil to germinate and for the release of seeds in the understory (Denslow, 1987). As seeds germinate and colonize the disturbed area, pioneer communities become dense due to the rapid generation of leaf area for maximized light interception, which contrasts with the surrounding mature forests that have a low leaf area density (Bazzaz & Pickett, 1980). Identifying dense light and water-dependent tropical rainforest canopy patches within areas ranging from <1 to >13 km^2 could be used to fingerprint relict retrogradational avulsion sites. These sites would also have fluvial landforms present (i.e., abandoned channels, alluvial ridges, scour marks, and topographical relief) from past flooding and sedimentation. This might serve to constrain the prevalence of retrogradational avulsions and their impact on species succession post-disturbance.

It remains to be seen, but retrogradational avulsions could emerge as an important disturbance regime in tropical rainforests. The disturbance size of a retrogradational avulsion is generally larger than other natural forest disturbance processes such as blowdowns (i.e., areas in which trees have been blown over by gusts of wind). In the Amazon, large blowdown events caused by convective cloud downdrafts (Garstang et al., 1998) destroy areas >0.3 km^2, with nearly all areas <5 km^2 and rare occurrences measured up to 33.7 km^2 (Nelson et al., 1994); however, small scale blowdown disturbances,

FIGURE 7 Total area of retrogradational avulsion floodplain disturbance produced by 19 retrogradational avulsions with labeled avulsion ID (from Edmonds et al., 2022), disturbance start and end year, and arrow representing downstream flow direction. Each different colored area represents the total disturbance produced within a 2-year period, with the earliest date superimposed over the later dates (color code shown in the bottom right corner). A time series analysis for avulsion disturbances with four or more 2-year periods is shown, with a single duration period representing 2 years (chart key shown in bottom right corner). [Color figure can be viewed at wileyonlinelibrary.com]

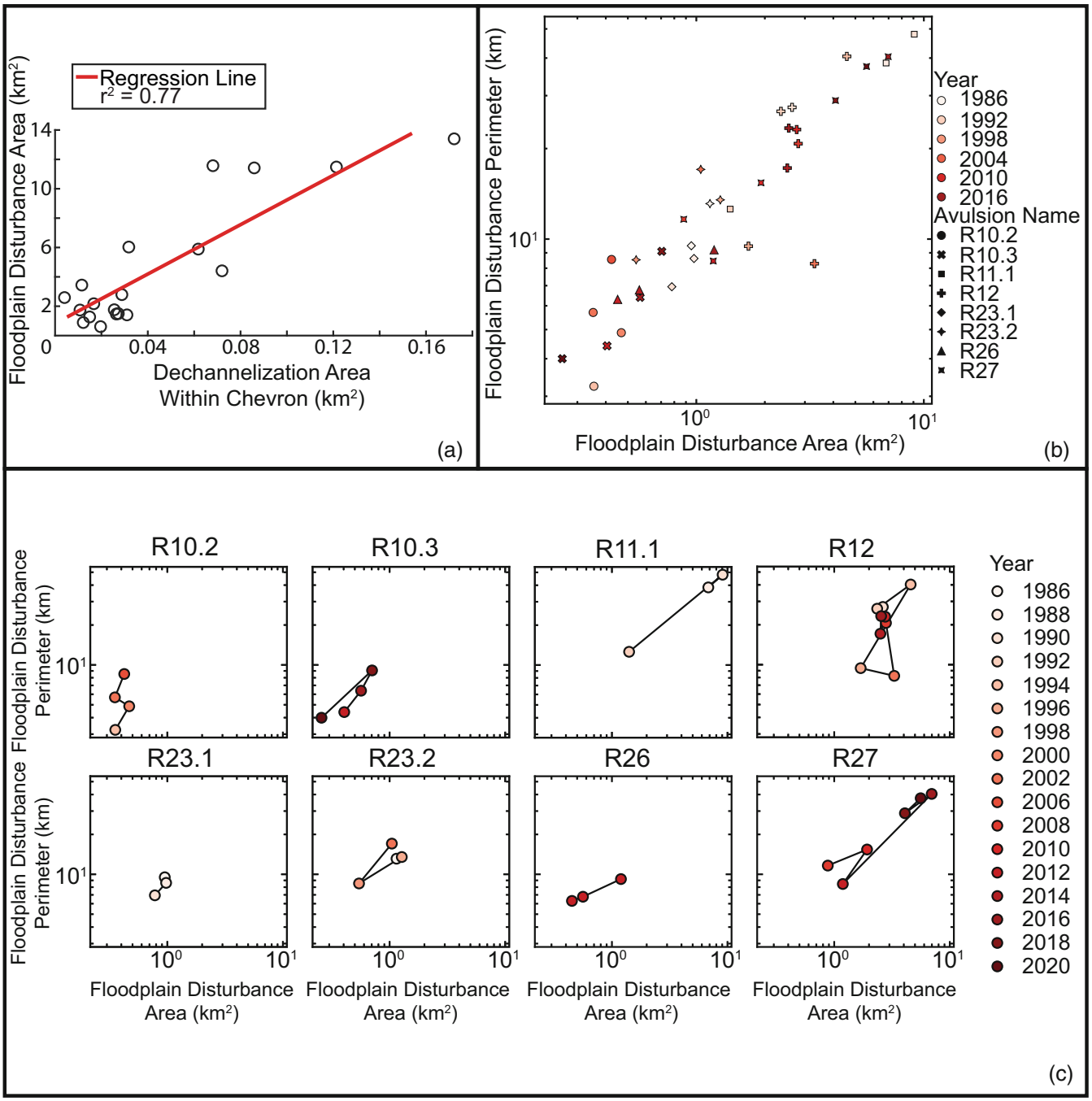

FIGURE 9 Selected scaling relationships for retrogradational avulsions. (a) The linear relationship between the floodplain disturbance area and dechannelization area within the chevron. (b) Log–log relationship between perimeter and area of floodplain disturbance for retrogradational avulsions for which we have at least three observations. Each avulsion example is represented by a different symbol; color denotes the year of the Landsat image (where darker shades are more recent). (c) Examples from (b) are shown in detail; the scale of axes in all eight subplots are the same, for comparison. Trajectories of floodplain disturbance perimeter and area over time indicated a persistent morphometric scaling relationship. [Color figure can be viewed at wileyonlinelibrary.com]

<0.001 km^2 per year, occur at ~10^7 orders of magnitude greater than large scale events >0.3 km^2 (Espírito-Santo et al., 2014). Blowdowns occur more frequently and over a larger spatial extent in the Amazon, while retrogradational avulsions, although surprisingly frequent, are typically larger: Edmonds et al. (2022) showed that 40% of the rivers had multiple retrogradational avulsions with an average recurrence interval of 9 years. Therefore, in certain areas, retrogradational avulsions may be as important as large blowdown events. Approximately 0.003 Pg C y^{-1} is released into the atmosphere by large blowdown events in the Amazon (Espírito-Santo et al., 2014) and if retrogradational avulsions have larger average disturbance areas, then the carbon released by the avulsion could be important in local settings.

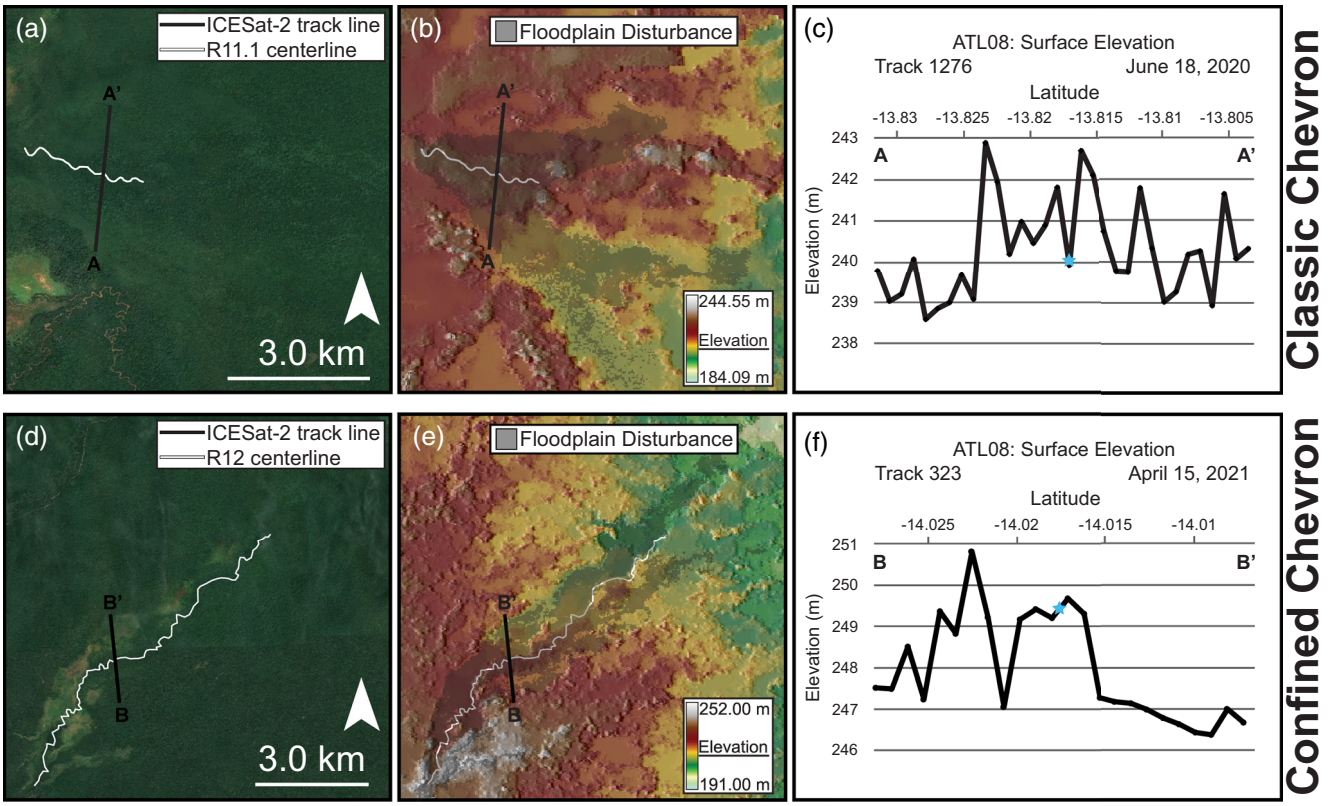

FIGURE 10 Topographic observations of rivers R11.1 (classic chevron disturbance structure) and R12 (confined chevron disturbance structure) in reference to retrogradational avulsion-related canopy gap evolution. (a, d) Current high-resolution satellite imagery from Google Earth Pro with river centerline and location of ICESat-2 ground track. (b, e) FABDEM hillshade with the transparent area of total floodplain disturbance produced by the retrogradational avulsion. (c, f) ATL08 surface elevation profile from the ICESat-2 satellite with track number and date of measurement on the floodplain (location of river channel identified as a blue star along profile). [Color figure can be viewed at wileyonlinelibrary.com]

4.3 | Topographic controls on flooding and floodplain disturbance

Our data and analysis did not pinpoint a clear control on what sets the disturbance area from a retrogradational avulsion. Given this, we hypothesize that floodplain topography controls the extent of retrogradational avulsion flooding, therefore influencing the geometry of floodplain disturbance in tropical forests. To test this idea, we used the 1 arc-second FABDEM (Forest And Buildings removed Copernicus DEM) dataset (Hawker et al., 2022) to co-analyze floodplain topography and associated disturbance. The FABDEM dataset is unique in that it has been tested on floodplains (Hawker et al., 2022); however, the DEM used for the FABDEM dataset, the Copernicus GLO-30 DEM, was surveyed between 2011 and 2015. During this time, some of the rivers studied in this paper underwent avulsion or were in the stabilization phase, which means the methodology from Hawker et al. (2022) would underestimate the elevation by assuming uniform vegetation in these locations with the surrounding canopy. To circumvent this issue, we used ICESat-2 surface elevation tracks near-perpendicular to the studied rivers obtained from ATL08 (land/vegetation) data measured by the Advanced Topographic Laser Altimeter System (ATLAS), a photon-counting lidar instrument, to provide additional topographic evidence that validated the FABDEM data (Neuenschwander & Pitts, 2019). Widespread cloud coverage in the Southeastern Papua and Amazon rainforests, data availability starting in 2018, and the orientation of the rivers with respect to the ICESat-2 ground tracks combined to greatly diminish available data for surface elevation on the floodplains. Due to the lack of data, we present two examples from retrogradational avulsions R11.1 and R12 to validate our hypothesis on topography influencing disturbance area.

In our analysis of the rivers, we found two distinct disturbance patterns, chevron-shaped and confined (Figure 7), and we suggest different topography controls the flooding extent shape (Figure 10). R11.1 exhibited the classic chevron pattern while R12 exhibited a more confined pattern. It seems that the chevron shape emerged during this process because of enhanced deposition around the channel during dechannelization. For instance, the higher topography between the downstream limbs of the chevron (Figure 10b) has a location of exceptional deposition (Lombardo, 2017). Deposition in this area caused the flow to split and form the chevron shape. Even without this extra deposition, flow splitting and chevron formation likely occurred because the channel had alluvial ridges with lower elevations on either side. This alluvial ridge helped disperse flood waters away from the channel.

The FABDEM suggested that the classic chevron resulted from wider topographic depressions while the confined chevron had much narrower depressions on either side of the river channel. The disturbance patterns had two limbs of unequal length. The southern limb of R11.1 and the northern limb of R12 both had steeper gradients that caused longer disturbance paths and provided further evidence that topographic influences determine size and structure. This initial analysis suggested that the area of disturbance probably depended on the topography and the lateral slopes that drive water away from the channel and out into the surrounding forest. More current and robust elevation data, along with detailed field study, are needed to further evaluate the role of floodplain topography in determining disturbance area.

5 | CONCLUSION

We presented detailed remotely sensed observations on land-cover change and floodplain disturbance in tropical rainforests caused by a new style of river avulsion called retrogradational avulsion. We measured morphological changes in the parent channel and migration rates of the sediment plug on a large retrogradational avulsion in Papua New Guinea identified as R3.2. On that avulsion, the sediment plug migrated upstream ~900 m over 6 years and in response, the parent channel doubled in width from 2003 to 2021. Using high-resolution satellite imagery, we quantified land-cover changes and identified four phases: flooding, channel breakout, channel establishment, and stabilization. During these phases, channel breakout had the largest vegetation die-off area, and channel establishment had the largest deposited sediment area on the floodplain. To understand more broadly how retrogradational avulsions disturb the floodplain, we expanded our scope to 19 retrogradational avulsions in parts of South America and Papua New Guinea. Using harmonized NDVI Landsat imagery, we found that the area of total disturbance associated with a single retrogradational avulsion in our sample ranged from <1 to >13 km^2, with the largest measured at 13.67 km^2. The floodplain disturbance area scaled with the dechannelization area within the chevron, disturbance area and perimeter trended toward consistent morphometry, and initial analyses suggested that the geometry of the disturbance was controlled by floodplain topography. We suggested that this new style of river avulsion has a greater disturbance extent, on average, than blowdown events. Our results suggested that floodplain models of tropical rainforest succession often overlook the significant role of retrogradational avulsions as an important disturbance regime. Further study is needed to better understand why retrogradational avulsions occur, what sets the size and shape of the associated disturbance, and how they might influence the patch mosaic structure of vegetation in forests.

ACKNOWLEDGMENTS

Riley T. Henson and Douglas A. Edmonds were supported by the U.S. National Science Foundation grant EAR-1911321. The authors also thank two anonymous reviewers for constructive comments that improved the manuscript.

DATA AVAILABILITY STATEMENT

The data that supports the findings of this study are available in the supplementary material of this article.

ORCID

Riley T. Henson https://orcid.org/0009-0002-8937-4393

REFERENCES

Assine, M. L., Macedo, H. A., Stevaux, J. C., Bergier, I., Padovani, C. R., & Silva, A. (2016). Avulsive rivers in the hydrology of the Pantanal wetland. *Dynamics of the Pantanal Wetland in South America*, *3*, 83–110. https://doi.org/10.1007/698_2015_351

Battisti, C., Poeta, G., & Fanelli, G. (2016). *An introduction to disturbance ecology* (pp. 13–29). Springer. https://doi.org/10.1007/978-3-319-32476-0

Bazzaz, F. A., & Pickett, S. T. A. (1980). Physiological ecology of tropical succession: A comparative review. *Annual Review of Ecology and Systematics*, *11*(1), 287–310. https://doi.org/10.1146/annurev.es.11.110180.001443

Bolstad, P., & Lillesand, T. M. (1991). Rapid maximum likelihood classification. *Photogrammetric Engineering and Remote Sensing*, *57*(1), 67–74.

Bottero, A., Garbarino, M., Dukic, V., Govedar, Z., Lingua, E., Nagel, T. A., & Motta, R. (2011). Gap-phase dynamics in the old-growth forest of Lom (Bosnia-Herzegovina). *Silva Fennica*, *45*, 875–887. https://doi.org/10.14214/sf.76

Brakenridge, G. R., Syvitski, J. P. M., Niebuhr, E., Overeem, I., Higgins, S. A., Kettner, A. J., & Prades, L. (2017). Design with nature: Causation and avoidance of catastrophic flooding, Myanmar. *Earth-Science Reviews*, *165*, 81–109. https://doi.org/10.1016/j.earscirev.2016.12.009

Bridge, J. S., & Leeder, M. R. (1979). A simulation model of alluvial stratigraphy. *Sedimentology*, *26*(5), 617–644. https://doi.org/10.1111/j.1365-3091.1979.tb00935.x

Brooke, S., Chadwick, A. J., Silvestre, J., Lamb, M. P., Edmonds, D. A., & Ganti, V. (2022). Where rivers jump course. *Science*, *376*(6596), 987–990. https://doi.org/10.1126/science.abm1215

Bryant, M., Falk, P., & Paola, C. (1995). Experimental study of avulsion frequency and rate of deposition. *Geology*, *23*(4), 365–368. https://doi.org/10.1130/0091-7613(1995)023<0365:ESOAFA>2.3.CO;2

Buehler, H. A., Weissmann, G. S., Scuderi, L. A., & Hartley, A. J. (2011). Spatial and temporal evolution of an avulsion on the Taquari River distributive fluvial system from satellite image analysis. *Journal of Sedimentary Research*, *81*(8), 630–640. https://doi.org/10.2110/jsr.2011.040

Chambers, J. Q., Negron-Juarez, R. I., Marra, D. M., Di Vittorio, A., Tews, J., Roberts, D., & Higuchi, N. (2013). The steady-state mosaic of disturbance and succession across an old-growth Central Amazon forest landscape. *Proceedings of the National Academy of Sciences*, *110*(10), 3949–3954. https://doi.org/10.1073/pnas.1202894110

Congalton, R. G. (1991). A review of assessing the accuracy of classifications of remotely sensed data. *Remote Sensing of Environment*, *37*(1), 35–46. https://doi.org/10.1016/0034-4257(91)90048-B

Denslow, J. S. (1987). Tropical rainforest gaps and tree species diversity. *Annual Review of Ecology and Systematics*, *18*(1), 431–451. https://doi.org/10.1146/annurev.es.18.110187.002243

Edmonds, D. A., Hajek, E. A., Downton, N., & Bryk, A. B. (2016). Avulsion flow-path selection on rivers in foreland basins. *Geology*, *44*(9), 695–698. https://doi.org/10.1130/G38082.1

Edmonds, D. A., Hoyal, D. C., Sheets, B. A., & Slingerland, R. L. (2009). Predicting delta avulsions: Implications for coastal wetland restoration. *Geology*, *37*(8), 759–762. https://doi.org/10.1130/G25743A.1

Edmonds, D. A., Martin, H. K., Valenza, J. M., Henson, R., Weissmann, G. S., Miltenberger, K., Mans, W., Moore, J. R., Slingerland, R. L., Gibling, M. R., Bryk, A. B., & Hajek, E. A. (2022). Rivers in reverse: Upstream-migrating dechannelization and flooding

cause avulsions on fluvial fans. *Geology*, *50*(1), 37–41. https://doi.org/10.1130/G49318.1

Espírito-Santo, F. D., Gloor, M., Keller, M., Malhi, Y., Saatchi, S., Nelson, B., Junior, R. C., Pereira, C., Lloyd, J., Frolking, S., Palace, M., Shimabukuro, Y. E., Duarte, V., Mendoza, A. M., López-González, G., Baker, T. R., Feldpausch, T. R., Brienen, R. J., Asner, G. P., … Phillips, O. L. (2014). Size and frequency of natural forest disturbances and the Amazon forest carbon balance. *Nature Communications*, *5*(1), 1–6. https://doi.org/10.1038/ncomms4434

Field, J. (2001). Channel avulsion on alluvial fans in southern Arizona. *Geomorphology*, *37*(1–2), 93–104. https://doi.org/10.1016/S0169-555X(00)00064-7

Flood, Y. S., & Hampson, G. J. (2014). Facies and architectural analysis to interpret avulsion style and variability: Upper cretaceous Blackhawk formation, Wasatch plateau, Central Utah, US aalluvial deposits as a record of avulsion style and variability. *Journal of Sedimentary Research*, *84*(9), 743–762. https://doi.org/10.2110/jsr.2014.59

Frolking, S., Palace, M. W., Clark, D. B., Chambers, J. Q., Shugart, H. H., & Hurtt, G. C. (2009). Forest disturbance and recovery: A general review in the context of spaceborne remote sensing of impacts on aboveground biomass and canopy structure. *Journal of Geophysical Research: Biogeosciences*, *114*(G2), 1–27. https://doi.org/10.1029/2008JG000911

Garstang, M., White, S., Shugart, H. H., & Halverson, J. (1998). Convective cloud downdrafts as the cause of large blowdowns in the Amazon rainforest. *Meteorology and Atmospheric Physics*, *67*, 199–212. https://doi.org/10.1007/BF01277510

Godoy, J. R., Petts, G., & Salo, J. (1999). Riparian flooded forests of the Orinoco and Amazon basins: A comparative review. *Biodiversity and Conservation*, *8*, 551–586. https://doi.org/10.1023/A:1008846531941

Gullison, R. E., Panfil, S. N., Strouse, J. J., & Hubbell, S. P. (1996). Ecology and management of mahogany (Swietenia macrophylla king) in the Chimanes Forest, Beni, Bolivia. *Botanical Journal of the Linnean Society*, *122*(1), 9–34. https://doi.org/10.1111/j.1095-8339.1996.tb02060.x

Hajek, E. A., & Edmonds, D. A. (2014). Is river avulsion style controlled by floodplain morphodynamics? *Geology*, *42*(3), 199–202. https://doi.org/10.1130/G35045.1

Hawker, L., Uhe, P., Paulo, L., Sosa, J., Savage, J., Sampson, C., & Neal, J. (2022). A 30 m global map of elevation with forests and buildings removed. *Environmental Research Letters*, *17*(2), 024016. https://doi.org/10.1088/1748-9326/ac4d4f

Hijmans, R. J., Cameron, S. E., Parra, J. L., Jones, P. G., & Jarvis, A. (2005). Very high resolution interpolated climate surfaces for global land areas. *International Journal of Climatology: A Journal of the Royal Meteorological Society*, *25*(15), 1965–1978. https://doi.org/10.1002/joc.1276

Hoyal, D. C. J. D., & Sheets, B. A. (2009). Morphodynamic evolution of experimental cohesive deltas. *Journal of Geophysical Research: Earth Surface*, *114*(F2), 1–18. https://doi.org/10.1029/2007JF000882

Hupp, C. R., & Osterkamp, W. R. (1985). Bottomland vegetation distribution along Passage Creek, Virginia, in relation to fluvial landforms. *Ecology*, *66*(3), 670–681. https://doi.org/10.2307/1940528

Iacobucci, G., Troiani, F., Milli, S., Mazzanti, P., Piacentini, D., Zocchi, M., & Nadali, D. (2020). Combining satellite multispectral imagery and topographic data for the detection and mapping of fluvial avulsion processes in lowland areas. *Remote Sensing*, *12*(14), 2243. https://doi.org/10.3390/rs12142243

Jerolmack, D. J., & Mohrig, D. (2007). Conditions for branching in depositional rivers. *Geology*, *35*(5), 463–466. https://doi.org/10.1130/G23308A.1

Jones, L. S., & Schumm, S. A. (1999). Causes of avulsion: An overview. In N. D. Smith, & J. Rogers (Eds.), *Fluvial sedimentology VI. Special publication 28* (pp. 171–178). International Association of Sedimentologists.

Kalliola, R., Salo, J., Puhakka, M., & Rajasilta, M. (1991). New site formation and colonizing vegetation in primary succession on the western Amazon floodplains. *The Journal of Ecology*, *79*, 877–901. https://doi.org/10.2307/2261087

Kumar, L., & Mutanga, O. (2018). Google earth engine applications since inception: Usage, trends, and potential. *Remote Sensing*, *10*(10), 1509. https://doi.org/10.3390/rs10101509

Lee, D. B., Martin, H. K., & Edmonds, D. A. (2022). A method to detect abrupt shifts in river channel position using a Landsat-derived water occurrence record. *Earth Surface Processes and Landforms*, *47*(15), 3546–3557. https://doi.org/10.1002/esp.5472

Lombardo, U. (2017). River logjams cause frequent large-scale forest die-off events in southwestern Amazonia. *Earth System Dynamics*, *8*(3), 565–575. https://doi.org/10.5194/esd-8-565-2017

Maezumi, S. Y., Elliott, S., Robinson, M., Betancourt, C. J., Gregorio de Souza, J., Alves, D., Grosvenor, M., Hilbert, L., Urrego, D. H., Gosling, W. D., & Iriarte, J. (2022). Legacies of indigenous land use and cultural burning in the Bolivian Amazon rainforest ecotone. *Philosophical Transactions of the Royal Society B*, *377*(1849), 20200499. https://doi.org/10.1098/rstb.2020.0499

Millard, C., Hajek, E., & Edmonds, D. A. (2017). Evaluating controls on crevasse-splay size: Implications for floodplain-basin filling. *Journal of Sedimentary Research*, *87*(7), 722–739. https://doi.org/10.2110/jsr.2017.40

Mohrig, D., Heller, P. L., Paola, C., & Lyons, W. J. (2000). Interpreting avulsion process from ancient alluvial sequences: Guadalope-Matarranya system (northern Spain) and Wasatch formation (western Colorado). *Geological Society of America Bulletin*, *112*(12), 1787–1803. https://doi.org/10.1130/0016-7606(2000)112%3C1787:IAPFAA%3E2.0.CO;2

Morón, S., Amos, K., Edmonds, D. A., Payenberg, T., Sun, X., & Thyer, M. (2017). Avulsion triggering by El Niño–Southern Oscillation and tectonic forcing: The case of the tropical Magdalena River, Colombia. *Bulletin*, *129*(9–10), 1300–1313. https://doi.org/10.1130/B31580.1

Myster, R. W. (2009). Plant communities of western Amazonia. *The Botanical Review*, *75*, 271–291. https://doi.org/10.1007/s12229-009-9032-1

Nelson, B. W., Kapos, V., Adams, J. B., Oliveira, W. J., & Braun, O. P. (1994). Forest disturbance by large blowdowns in the Brazilian Amazon. *Ecology*, *75*, 853–858. https://doi.org/10.2307/1941742

Neuenschwander, A., & Pitts, K. (2019). The ATL08 land and vegetation product for the ICESat-2 Mission. *Remote Sensing of Environment*, *221*, 247–259. https://doi.org/10.1016/j.rse.2018.11.005

Olson, D. M., Dinerstein, E., Wikramanayake, E. D., Burgess, N. D., Powell, G. V., Underwood, E. C., D'amico, J. A., Itoua, I., Strand, H. E., Morrison, J. C., Loucks, C. J., Allnutt, T. F., Ricketts, T. H., Kura, Y., Lamoreux, J. F., Wettengel, W. W., Hedao, P., & Kassem, K. R. (2001). Terrestrial ecoregions of the world: A new map of life on EarthA new global map of terrestrial ecoregions provides an innovative tool for conserving biodiversity. *Bioscience*, *51*(11), 933–938. https://doi.org/10.1641/0006-3568(2001)051[0933:TEOTWA]2.0.CO;2

Pires, J. M., & Prance, G. T. (1985). The vegetation types of the Brazilian Amazon. In G. T. Prance & T. E. Lovejoy (Eds.), *Key environments: Amazonia* (pp. 110–145). Pergamon Pr.

Poorter, L., & Hayashida-Oliver, Y. (2000). Effects of seasonal drought on gap and understorey seedlings in a Bolivian moist forest. *Journal of Tropical Ecology*, *16*(4), 481–498. https://doi.org/10.1017/S026646740000153X

Richards, K., Brasington, J., & Hughes, F. (2002). Geomorphic dynamics of floodplains: Ecological implications and a potential modelling strategy. *Freshwater Biology*, *47*(4), 559–579. https://doi.org/10.1046/j.1365-2427.2002.00920.x

Roy, D. P., Kovalskyy, V., Zhang, H. K., Vermote, E. F., Yan, L., Kumar, S. S., & Egorov, A. (2016). Characterization of Landsat-7 to Landsat-8 reflective wavelength and normalized difference vegetation index continuity. *Remote Sensing of Environment*, *185*, 57–70. https://doi.org/10.1016/j.rse.2015.12.024

Simon, A., & Darby, S. E. (1997). Process-form interactions in unstable sand-bed river channels: A numerical modeling approach. *Geomorphology*, *21*(2), 85–106. https://doi.org/10.1016/S0169-555X(97)00043-3

Singh, M., Sood, S., & Collins, C. M. (2022). Fire dynamics of the Bolivian Amazon. *Land*, *11*(9), 1436. https://doi.org/10.3390/land11091436

Slingerland, R., & Smith, N. D. (1998). Necessary conditions for a meandering-river avulsion. *Geology*, *26*(5), 435–438. https://doi.org/10.1130/0091-7613(1998)026%3C0435:NCFAMR%3E2.3.CO;2

Slingerland, R., & Smith, N. D. (2004). River avulsions and their deposits. *Annual Review of Earth and Planetary Sciences*, *32*, 257–285. https://doi.org/10.1146/annurev.earth.32.101802.120201

Smith, N. D., Cross, T. A., Dufficy, J. P., & Clough, S. R. (1989). Anatomy of an avulsion. *Sedimentology*, *36*(1), 1–23. https://doi.org/10.1111/j.1365-3091.1989.tb00817.x

Stanford, J. A., Lorang, M. S., & Hauer, F. R. (2005). The shifting habitat mosaic of river ecosystems. *Internationale Vereinigung für Theoretische Und Angewandte Limnologie: Verhandlungen*, *29*(1), 123–136. https://doi.org/10.1080/03680770.2005.11901979

Syvitski, J. P., & Brakenridge, G. R. (2013). Causation and avoidance of catastrophic flooding along the Indus River, Pakistan. *GSA Today*, *23*(1), 4–10. https://doi.org/10.1130/GSATG165A.1

Tockner, K., Lorang, M. S., & Stanford, J. A. (2010). River flood plains are model ecosystems to test general hydrogeomorphic and ecological concepts. *River Research and Applications*, *26*(1), 76–86. https://doi.org/10.1002/rra.1328

Valente, C. R., Latrubesse, E. M., & Ferreira, L. G. (2013). Relationships among vegetation, geomorphology and hydrology in the Bananal Island tropical wetlands, Araguaia River basin, Central Brazil. *Journal of South American Earth Sciences*, *46*, 150–160. https://doi.org/10.1016/j.jsames.2012.12.003

Valenza, J. M., Edmonds, D. A., Hwang, T., & Roy, S. (2020). Downstream changes in river avulsion style are related to channel morphology. *Nature Communications*, *11*(1), 2116. https://doi.org/10.1038/s41467-020-15859-9

Valenza, J. M., Edmonds, D. A., & Weissmann, G. S. (2022). Quantifying river avulsion activity from satellite remote sensing: Implications for how avulsions contribute to floodplain stratigraphy in foreland basins. *Journal of Sedimentary Research*, *92*(6), 487–502. https://doi.org/10.2110/jsr.2021.038

Van Asselen, S., Cohen, K. M., & Stouthamer, E. (2017). The impact of avulsion on groundwater level and peat formation in delta floodbasins during the middle-Holocene transgression in the Rhine-Meuse delta, The Netherlands. *The Holocene*, *27*(11), 1694–1706. https://doi.org/10.1177/0959683617702224

Ward, J. V., Tockner, K., Arscott, D. B., & Claret, C. (2002). Riverine landscape diversity. *Freshwater Biology*, *47*(4), 517–539. https://doi.org/10.1046/j.1365-2427.2002.00893.x

Wittmann, F., Schöngart, J., Montero, J. C., Motzer, T., Junk, W. J., Piedade, M. T., Queiroz, H. L., & Worbes, M. (2006). Tree species composition and diversity gradients in white-water forests across the Amazon Basin. *Journal of Biogeography*, *33*(8), 1334–1347. https://doi.org/10.1111/j.1365-2699.2006.01495.x

World Bank Group. (2022). *Climate Change Knowledge Portal*. https://climateknowledgeportal.worldbank.org/

SUPPORTING INFORMATION

Additional supporting information can be found online in the Supporting Information section at the end of this article.

How to cite this article: Henson, R. T., Edmonds, D. A., & Lazarus, E. D. (2024). Remotely sensed land-cover change and floodplain disturbance following upstream-migrating river avulsions in tropical rainforests. *River Research and Applications*, *40*(4), 559–574. https://doi.org/10.1002/rra.4256